JOURNAL OF GUIDANCE, CONTROL, AND DYNAMICS
Vol. 28, No. 4, July–August 2005

Magnetometer-Based Attitude and Rate Estimation for Spacecraft with Wire Booms

Todd E. Humphreys,* Mark L. Psiaki,† Eric M. Klatt,‡ Steven P. Powell,§ and Paul M. Kintner Jr.¶
Cornell University, Ithaca, New York 14853-7501

A magnetometer-based filter and smoother are presented for estimating attitude, rate, and boom orientations for a spinning spacecraft that has wire booms. These estimates are needed to analyze science data from the subpayloads of a recent sounding rocket mission. The estimator is initialized with the measured angular rate of each subpayload at ejection and thereafter relies solely on three-axis magnetometer data. The estimation process is complicated by the flexible wire booms whose full parameterization for even the simplest pendulous modes would require 16 state elements. Several simplifying assumptions about the motion of the booms reduce the problem's complexity. A magnetometer-based attitude and rate estimator is developed that is suited to the time-varying model errors resulting from these assumptions. The estimator uses inertial angular momentum in place of angular rate in its state vector, and it explicitly includes an error model for its approximate relationship between angular rate and angular momentum. The estimator, a filter/smoother, is applied to synthetic data from a truth-model simulator and then to actual telemetry from the mission subpayloads. Accuracies are on the order of several degrees. The estimator is applicable whenever Euler-type equations must be used to propagate rate estimates in the presence of significant dynamics modeling errors.

I. Introduction

THE present work draws its impetus from the sounding rocket experiment Sounding of the Ion Energization Region: Resolving Ambiguities (SIERRA), launched from Poker Flat, Alaska, in January 2002. Roughly 350 s before apogee, the primary SIERRA payload ejected two smaller spacecraft at an interval of 33 s between ejections. The three spin-stabilized payloads continued along a ballistic trajectory, finally reaching apogee at 735 km before falling Earthward. Total flight time was about 950 s (Ref. 1). The separate payloads were essential to resolving a temporal/spatial ambiguity in electric field measurements of the ionosphere. Also critical was a broad measurement baseline for each payload. Mission specifications called for four probes extending radially from each payload's nominal axis of rotation, with opposing probes separated by 6 m. This was a challenge particularly for the subpayloads, whose compactness barred the use of rigid booms. SIERRA designers ultimately satisfied the opposing broad baseline and compactness requirements via the Cornell wire-boom yo-yo system.[2,3] Probes were connected to flexible cables wound helically around an articulating drum and then spun out during flight in a yo-yo-type deployment that was controlled by a damper.

An estimate of spacecraft attitude and boom orientations for each payload enables researchers to correlate telemetry with spatial features of the background electric field. For the primary payload, with rigid booms and a comprehensive attitude sensor suite consisting of inertial sensors and a three-axis magnetometer (TAM), formulating an attitude estimate is conceptually straightforward. The subpayloads present more of a challenge. Much more compact and lighter than the primary payload, their only attitude sensor is an onboard TAM. Each TAM measurement provides two axes of attitude information. This is insufficient for single-frame attitude estimation, obliging reliance on both an Euler model, for propagation of the spacecraft dynamics between measurements, and an initial estimate of the angular momentum vector. The complex dynamics of the flexible wire booms are difficult to incorporate directly into an estimation algorithm. Therefore, modeling approximations are used, but these introduce uncertainty into the Euler model. The estimation challenge for the subpayloads is tersely restated in the following terms: Three-axis attitude, rate, and boom orientation estimates are desired in the face of significant time-varying modeling uncertainty and weak observability about one axis.

Previous research efforts have produced various results that can be used to synthesize a solution to the SIERRA subpayload attitude estimation problem. A general dynamics analysis of spacecraft employing wire-boom antennas was presented in Ref. 4. Work on another sounding rocket mission recognized the challenges posed by structural flexibility in Euler-based attitude and rate estimation.[5] In particular, it was found that rigid-body models are inadequate when significant flexible modes are present. In contrast to the present case, however, the sounding rocket described in Ref. 5 was equipped with semirigid booms and multiple attitude sensors that provided data during most of its flight.

A substantial body of research has dealt with magnetometer-only attitude estimation applied to rigid spacecraft.[6–10] These methods rely on accurate Euler models of the spacecraft dynamics because of the lack of rate-gyro data. The Euler models are used to estimate attitude rates and to observe the attitude about the axis that is not already sensed. These models assume accurate prior knowledge of the spacecraft inertial parameters. In Ref. 9, it is demonstrated that estimates of inertia matrix parameters may be refined by including these as part of the estimated state. This applies, however, to the inertia parameters of a rigid body. A similar approach would be unworkable in the present case due to the complexity of the wire-boom system. Many of the flexible-body modes are themselves unobservable purely from magnetometer data, and a significant number of the inertial parameters, such as the tip-mass values, are equally unobservable.

Attitude observability for magnetometer-based estimation is dependent on movement of the local magnetic field vector's direction in inertial space. This movement is primarily a consequence of the spacecraft's motion along its orbit. An additional challenge for SIERRA attitude estimation is that the sounding rocket trajectory is

---

Received 19 January 2004; revision received 6 July 2004; accepted for publication 10 July 2004.

*Graduate Student, Sibley School of Mechanical and Aerospace Engineering. Student Member AIAA.

†Associate Professor, Sibley School of Mechanical and Aerospace Engineering. Associate Fellow AIAA.

‡Graduate Student, School of Electrical and Computer Engineering.

§Senior Engineer, School of Electrical and Computer Engineering.

¶Professor, School of Electrical and Computer Engineering. Senior Member AIAA.

short. Over the course of the 700-s data capture phase, the magnetic field moves only 13.6 deg in inertial coordinates.

A consequence of this condition is increased reliance on an initial estimate of each subpayload's angular momentum vector. These estimates are provided at separation by inertial sensors onboard the primary payload. The low level of external torques for the SIERRA mission implies that the angular momentum vector for each subpayload remains nearly fixed in inertial space. Therefore, the initial angular momentum acts almost like an independent attitude reference throughout the duration of the flight.

The filter and smoother developed in this paper are Euler-based estimators that exploit prior knowledge of the spacecraft angular momentum while gracefully accommodating errors that arise from unmodeled torques and from approximation of the effects of the flexible modes. The estimated state vector in the new filter/smoother directly includes the angular momentum components in inertial coordinates in place of the more common angular rate vector. The benefit of this approach is that, because of conservation of angular momentum, the prediction step for this vector is essentially trivial. This is important because modeling errors, when coupled with nonlinearities, would otherwise bleed into the rate propagation and ultimately express themselves in a wandering inertial angular momentum vector. This unforced wander is undesirable especially when one axis is weakly observable, as in the present case, because errors accumulating about the weakly observable axis are not easily corrected.

Euler-model errors are accommodated in the estimator by including a random uncertainty model for the relationship between the angular rate and the angular momentum in spacecraft coordinates. This extra source of random uncertainty is important in the present problem for the following reason: The significant effects of the spacecraft's flexible modes are included through an approximate relationship between angular velocity and angular momentum that is tailored to be relatively accurate for the dominant mode of motion. This dominant mode is the flexible-body equivalent of the nutation mode of a rigid minor-axis spinner. The random uncertainty model is included in the spacecraft kinematics exactly where the approximate angular-rate/angular-momentum relationship is invoked. This approach more accurately models the way errors are introduced into the Euler model than does, for example, a simple increase of the modeled disturbance torque.

The three main contributions of this paper to attitude estimation techniques are 1) use of the inertially referenced angular momentum components in the state vector in place of the body-referenced angular velocity components, 2) inclusion of a random error model in the angular-momentum/angular-velocity relationship, and 3) an approximate angular-momentum/angular-velocity relationship that is valid for unstable nutation of a spinning spacecraft with flexible wire booms. These contributions are key to successful magnetometer-based attitude estimation for spinning spacecraft with wire booms. Their utility is demonstrated by successful application of a filter and a smoother employing these techniques to the problem of the SIERRA subpayloads. Contributions 1 and 2 should also prove useful for Euler-based attitude and rate estimation for any spacecraft if there is significant modeling uncertainty in the Euler dynamics model.

The balance of this paper is laid out as follows. A mathematical model of the flexible spacecraft motion is presented in Sec. II, and several simplifying assumptions are motivated and used to develop a relationship between the angular momentum and the angular velocity. In Sec. III is provided a summary of the attitude parameterization used, then the estimator is developed. The estimator is evaluated in Sec. IV with synthetic data from a truth-model simulation, and it is evaluated in Sec. V with data telemetered from the SIERRA subpayloads. In Sec. VI other situations in which the paper's techniques apply are considered, and in Sec. VII the paper's conclusions are presented.

II. Flexible-Body Model and Simplifying Assumptions

The essential features of the deployed SIERRA subpayloads are shown in Fig. 1. Four 3-m wire booms nominally spanning a plane are oriented radially about the spin axis. The articulating upper drum, which is used to control the unwinding of the wire booms during deployment and about which the wire booms are wrapped in the stowed configuration, is held fast by a locking brake after deployment. This implies that the drum and the main spacecraft body may be modeled as a single rigid body. The center of mass of this rigid body constitutes the origin of the spacecraft-body reference frame. The body z axis z_b is aligned along the nominal spin axis. When the flexible booms are added, a system center of mass may be defined, which is, in general, slightly displaced from the center of mass of the main-body-plus-drum system. The translational motion of the system center of mass is independent of attitude, and this fact can be used to advantage when deriving the equations governing the attitude dynamics. Attitude is measured with respect to an inertial reference frame whose axes are aligned with those of the mean J2000 Earth-centered inertial reference frame. The system angular momentum is given as the vector $\boldsymbol{h}$. Boom vibrational modes beyond the first-order (pendulous) mode are assumed to be negligible. This is a good approximation for the SIERRA subpayloads.[2–4] Hence, the physical wire booms, which are flexible all along their length, are modeled as simple pendulums for purposes of simulation and estimation. In this work, both the physical booms and their model are described as flexible because their positions can deform with respect to spacecraft coordinates. Out-of-plane and in-plane deflections of the ith boom are denoted by the angles ϕ_i and γ_i. Note that this represents a notational shift from Refs. 2 and 3, wherein θ_i is the in-plane boom deflection.

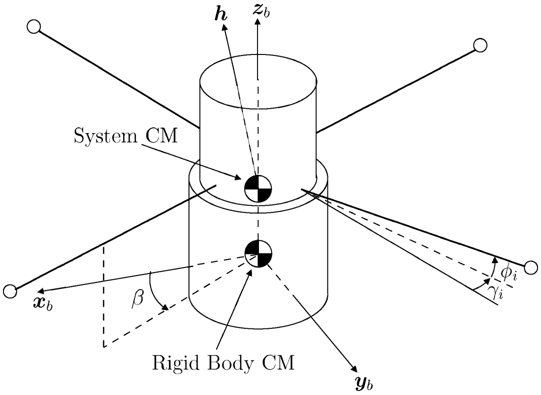

Fig. 1 Geometry of the SIERRA subpayloads.

A comprehensive dynamics model for a general case with N booms is found in Ref. 2. This may be used to construct, for the four-boom case, a dynamics model of the form $\dot{\boldsymbol{x}} = f(\boldsymbol{x}, \boldsymbol{n})$ governing the time evolution of a 23-element state vector $\boldsymbol{x}$. The state vector is composed of the angular rate vector of the rigid body $\boldsymbol{\omega}$, the attitude quaternion $\boldsymbol{q}$, the angles ϕ_i and γ_i, and their first time derivatives:

$$\boldsymbol{x} = \left[\boldsymbol{\omega}^T, \boldsymbol{q}^T, \phi_1, \dot{\phi}_1, \gamma_1, \dot{\gamma}_1, \ldots, \phi_4, \dot{\phi}_4, \gamma_4, \dot{\gamma}_4\right]^T \tag{1}$$

External torques act on the system through the vector $\boldsymbol{n}$.

Insight into the behavior of the spacecraft and flexible booms is had by linearizing $f(\boldsymbol{x}, \boldsymbol{n})$ about a nominal state and examining the characteristic motion of the linearized system. The SIERRA subpayloads nominally rotate about the z_b axis at an angular rate of 1.7 Hz. The in- and out-of-plane angles γ_i and ϕ_i and their first time derivatives are nominally zero. Linearization about these nominal values (and a chosen $\boldsymbol{q}$) yields a linearized dynamics model of the form $\Delta\dot{\boldsymbol{x}} = F\Delta\boldsymbol{x}$ valid for small perturbations about the nominal values. Eigenvalue analysis of the linearized dynamics matrix F reveals a slightly unstable nutational mode, a result of design constraints that leave the subpayloads spinning about the rigid-body equivalent of their minor inertia axes. As a consequence, energy dissipation in the flexible booms drives an increase in the spacecraft nutation angle (the angle between $\boldsymbol{h}$ and z_b) and leads finally to rotation about the equivalent of the major rigid-body inertia axis. Because of the short duration of the flight, the unstable mode and consequent slow growth of the nutation angle were considered acceptable.[3]

The rate of growth of the unstable mode and the decay time constants of the stable modes are functions of the energy dissipated by bending in the booms. A lumped dissipation parameter was calculated for the SIERRA subpayloads in pre- and postlaunch empirical studies, predicting stable mode time constants of less than 300 s (Refs. 2 and 3). Immediately following boom deployment, spacecraft motion may be expected to contain contributions from several different modes. Within a short interval the nutational mode dominates as the stable modes die out.

An important feature of the nutational mode in the SIERRA design is that, as long as the nutation angle is small (<15 deg), in-plane displacements of the wire booms are very small ($<\frac{1}{2}$ deg). Moreover, to a very good approximation, the booms remain perpendicular to the angular momentum vector (within $\frac{1}{2}$ deg). When this perpendicularity approximation is used, the angles ϕ_i and rates $\dot{\phi}_i$ can be estimated if $\boldsymbol{h}$ is known in spacecraft body coordinates (call the latter quantity $\boldsymbol{h}_{\text{sc}}$). These features of boom motion motivate the following approximations that greatly simplify the spacecraft dynamics model:

$$\gamma_i = \dot{\gamma}_i = 0, \qquad i = 1, \dots, 4 \tag{2}$$

$$\boldsymbol{c}_i^T \boldsymbol{h}_{\text{sc}} = 0, \qquad i = 1, \dots, 4 \tag{3}$$

Here, the unit vector $\boldsymbol{c}_i = \boldsymbol{c}_i(\phi_i)$ is aligned along the ith boom.

An implicit relationship between $\boldsymbol{h}_{\text{sc}}$, $\boldsymbol{\omega}$, and the boom angles ϕ_i and rates $\dot{\phi}_i$ follows from these simplifying assumptions. First, angular momentum about the system center of mass is expressed in body coordinates as

$$\boldsymbol{h}_{\text{sc}} = -m_b(\boldsymbol{r}_{\text{cm}} \times \boldsymbol{v}_b) + J_b\boldsymbol{\omega} + \sum_{i=1}^{4} m_i(\boldsymbol{r}_i - \boldsymbol{r}_{\text{cm}}) \times \boldsymbol{v}_i \tag{4}$$

under the following definitions, where all vectors are in body coordinates:

m_b = mass of the main spacecraft body plus drum

$\boldsymbol{r}_{\text{cm}}$ = vector from the main body/drum c.m. to the system c.m., $= \boldsymbol{r}_{\text{cm}}(\phi_1, \phi_2, \phi_3, \phi_4)$

$\boldsymbol{v}_b$ = inertial velocity of the main body/drum c.m., $= \boldsymbol{v}_b(\phi_1, \dots, \phi_4, \dot{\phi}_1, \dots, \dot{\phi}_4)$

J_b = moment-of-inertia matrix of the main body/drum

m_i = effective tip mass of the ith boom (includes one-third of the mass of the ith cable)

$\boldsymbol{r}_i$ = vector from the main body/drum c.m to the ith tip mass, $= \boldsymbol{r}_i(\phi_i)$

$\boldsymbol{v}_i$ = inertial velocity of the ith tip mass, $= \boldsymbol{v}_i(\phi_1, \dots, \phi_4, \dot{\phi}_1, \dots, \dot{\phi}_4)$

The functions $\boldsymbol{r}_{\text{cm}}(\phi_1, \dots, \phi_4)$, $\boldsymbol{v}_b(\phi_1, \dots, \phi_4, \dot{\phi}_1, \dots, \dot{\phi}_4)$, $\boldsymbol{r}_i(\phi_i)$, $\boldsymbol{v}_i(\phi_1, \dots, \phi_4, \dot{\phi}_1, \dots, \dot{\phi}_4)$, and $\boldsymbol{c}_i(\phi_i)$ are all defined in Ref. 2.

Second, the approximation of Eq. (3), repeated here for convenience, is considered together with its first time derivative:

$$\boldsymbol{c}_i^T(\phi_i)\boldsymbol{h}_{\text{sc}} = 0, \qquad i = 1, \dots, 4 \tag{5}$$

$$\dot{\phi}_i \left[\frac{\mathrm{d}\boldsymbol{c}_i}{\mathrm{d}\phi_i}\right]^T \boldsymbol{h}_{\text{sc}} + \boldsymbol{c}_i^T(\phi_i)[-\boldsymbol{\omega} \times \boldsymbol{h}_{\text{sc}}] = 0, \qquad i = 1, \dots, 4 \tag{6}$$

where the second term on the left-hand side of Eq. (6) assumes that $\dot{\boldsymbol{h}}_{\text{sc}} = -\boldsymbol{\omega} \times \boldsymbol{h}_{\text{sc}}$, which is true if external torque is zero. Equation (5) implicitly defines (under mild smoothness conditions) each ϕ_i in terms of $\boldsymbol{h}_{\text{sc}}$:

$$\phi_i = \phi_i(\boldsymbol{h}_{\text{sc}}), \qquad i = 1, \dots, 4 \tag{7}$$

Thus, given $\boldsymbol{h}_{\text{sc}}$, one can solve for each ϕ_i and, hence, each $\boldsymbol{c}_i(\phi_i)$. Substitution into Eq. (6) yields $\dot{\phi}_i$ as a function of $\boldsymbol{h}_{\text{sc}}$ and as a linear function of $\boldsymbol{\omega}$:

$$\dot{\phi}_i = \dot{\phi}_i(\boldsymbol{h}_{\text{sc}}, \boldsymbol{\omega}), \qquad i = 1, \dots, 4 \tag{8}$$

With these relations, the vectors on the right-hand side of Eq. (4) may be written in terms of $\boldsymbol{h}_{\text{sc}}$ and $\boldsymbol{\omega}$, and the resulting equation takes the form

$$\boldsymbol{h}_{\text{sc}} = J(\boldsymbol{h}_{\text{sc}})\boldsymbol{\omega} \tag{9}$$

This form arises because of the linear dependence of $\boldsymbol{v}_b$ and $\boldsymbol{v}_i$ on $\dot{\phi}_1, \dots, \dot{\phi}_4$ and $\boldsymbol{\omega}$. The matrix function $J(\boldsymbol{h}_{\text{sc}})$ is effectively an angular momentum-dependent moment-of-inertia matrix. Equation (9) may be inverted to yield $\boldsymbol{\omega}$ as a function of $\boldsymbol{h}_{\text{sc}}$:

$$\boldsymbol{\omega}(\boldsymbol{h}_{\text{sc}}) = J^{-1}(\boldsymbol{h}_{\text{sc}})\boldsymbol{h}_{\text{sc}} \tag{10}$$

III. Estimator Development

Attitude Representation

The magnetic field is the sole attitude measurement for the SIERRA subpayloads after separation from the primary payload. Hence, the greatest attitude uncertainty is in rotation and rate about the magnetic field vector. In Ref. 9, a three-parameter attitude representation is developed that isolates rotation about the measured magnetic field vector in a single parameter θ. Two other attitude parameters, α_1 and α_2, are used to account for magnetometer measurement noise. The full attitude parameterization is $\{\alpha_1, \alpha_2, \theta\}$ and may be introduced in the following manner:

If $\hat{\boldsymbol{b}}_{\text{sc}}$ is the unit vector in the direction of the measured magnetic field in the spacecraft reference frame and $\hat{\boldsymbol{b}}_{\text{in}}$ is the unit vector in the direction of the magnetic field in the inertial reference frame, then the quaternion relating the two reference frames is parameterized as

$$\boldsymbol{q}(\alpha_1, \alpha_2, \theta) = \frac{1}{\sqrt{1 + \alpha_1^2 + \alpha_2^2}} \begin{bmatrix} \alpha_1\hat{\boldsymbol{v}}_1 + \alpha_2\hat{\boldsymbol{v}}_2 \\ 1 \end{bmatrix} \otimes \begin{bmatrix} \hat{\boldsymbol{b}}_{\text{sc}}\sin(\theta/2) \\ \cos(\theta/2) \end{bmatrix}$$
$$\otimes\, \boldsymbol{q}_{\min}(\hat{\boldsymbol{b}}_{\text{sc}}, \hat{\boldsymbol{b}}_{\text{in}}) \tag{11}$$

where $\hat{\boldsymbol{v}}_{1,2}$ are unit vectors that, together with $\hat{\boldsymbol{b}}_{\text{sc}}$, form a right-hand orthonormal triad and the symbol $\otimes$ denotes quaternion composition. The minimum quaternion $\boldsymbol{q}_{\min}(\hat{\boldsymbol{b}}_{\text{sc}}, \hat{\boldsymbol{b}}_{\text{in}})$ is the quaternion of minimum rotation that maps $\hat{\boldsymbol{b}}_{\text{in}}$ into $\hat{\boldsymbol{b}}_{\text{sc}}$.

Figure 2 shows the rotations associated with each attitude parameter. The parameter θ corresponds to a rotation about the measured magnetic field vector in spacecraft coordinates. The parameters α_1 and α_2 correspond to respective rotations about axes $\hat{\boldsymbol{v}}_1$ and $\hat{\boldsymbol{v}}_2$. Note, by Eq. (11), that α_1 and α_2 approximately equal one-half of the total rotation about $\hat{\boldsymbol{v}}_1$ and $\hat{\boldsymbol{v}}_2$, respectively. This can be seen by comparing the first quaternion on the right-hand side of Eq. (11) with the general form of the quaternion in which the axis of rotation is scaled by the factor $\sin(\theta/2)$, which, in the small-angle approximation, is one-half of the rotation angle θ. When combined in Eq. (11) under the small-angle approximation, α_1 and α_2 produce a total rotation angle of $2\sqrt{(\alpha_1^2 + \alpha_2^2)}$ about the rotation vector $\alpha_1\hat{\boldsymbol{v}}_1 + \alpha_2\hat{\boldsymbol{v}}_2$ to correct for errors in $\hat{\boldsymbol{b}}_{\text{sc}}$, as shown in Fig. 2.

The attitude singularity associated with this three-parameter attitude representation occurs at 180-deg rotation about any vector perpendicular to the measured magnetic field. It is avoided because α_1 and α_2, which represent rotation about vectors perpendicular to $\boldsymbol{b}_{\text{sc}}$, also parameterize the magnetometer measurement errors. Small

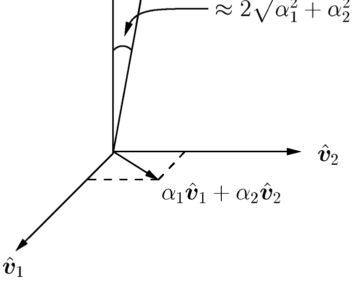

Fig. 2 Attitude parameters θ, α_1, and α_2 and their corresponding rotation angles.

magnetometer measurement errors lead to small values for α_1 and α_2, and the singularity is avoided.

One advantage of this parameterization is that, as will be seen in a later section, it provides for a simple model relating magnetic field measurements to spacecraft attitude.

Estimator State Vector

The state vector of the new filter/smoother is

$$\boldsymbol{x} = \left[\boldsymbol{h}_{\text{in}}^T, \alpha_1, \alpha_2, \theta\right]^T \tag{12}$$

where angular momentum expressed in inertial coordinates has been included with the attitude parameterization of the preceding section. The inclusion of $\boldsymbol{h}_{\text{in}}$ represents a departure from typical state vectors used to estimate spacecraft attitude and rate. These commonly employ angular rate $\boldsymbol{\omega}$ instead of $\boldsymbol{h}_{\text{in}}$. The rationale behind this replacement will become clear in later sections as the estimator is formulated and tested.

Note that the state vector presented here is sufficient to describe the angular rate of the rigid body and the boom orientations, provided the simplifying assumptions of Eqs. (2) and (3) are valid. This can be seen by using the attitude parameterization to map $\boldsymbol{h}_{\text{in}}$ into spacecraft body coordinates,

$$\boldsymbol{h}_{\text{sc}} = A[\boldsymbol{q}(\alpha_1, \alpha_2, \theta)]\boldsymbol{h}_{\text{in}}$$

where $A[\boldsymbol{q}]$ is the direction-cosine matrix equivalent of the quaternion $\boldsymbol{q}$. The function $\boldsymbol{\omega}(\boldsymbol{h}_{\text{sc}})$ is then used to compute $\boldsymbol{\omega}$ in body coordinates. Finally, out-of-plane boom angles ϕ_i are calculated using Eq. (7), and in-plane boom angles γ_i are assumed to be zero, following the assumption in Eq. (2).

State Observability

A brief discussion of state observability will aid understanding of the filter and smoother behavior. Any single magnetometer measurement provides only two axes of attitude information, but a series of measurements is, under modest conditions, sufficient for full attitude and rate observability. The reasoning for this is as follows. Except under very restrictive circumstances (when the spacecraft angular momentum vector and the magnetic field are aligned), the angular rate $\boldsymbol{\omega}$ is observable from a series of vector magnetometer measurements.[10] The spacecraft-referenced angular momentum $\boldsymbol{h}_{\text{sc}}$ can then be calculated using Eq. (9). If the spacecraft location is known (by using an onboard global positioning system receiver, for example), the vector $\hat{\boldsymbol{b}}_{\text{in}}$ may be calculated using a geomagnetic field model. The vector $\hat{b}_{\text{sc}}$ is given by magnetometer measurements. If the vector $\boldsymbol{h}_{\text{in}}$ were also known, the set $\{\boldsymbol{h}_{\text{sc}}, \boldsymbol{h}_{\text{in}}, \hat{\boldsymbol{b}}_{\text{sc}}, \hat{\boldsymbol{b}}_{\text{in}}\}$ would completely determine the spacecraft attitude $\{\alpha_1, \alpha_2, \theta\}$, provided $\boldsymbol{h}_{\text{in}}$ and $\hat{\boldsymbol{b}}_{\text{in}}$ were not aligned. This well-known result is embodied in the algebraic (TRIAD) method of attitude determination.[11] State observability is thus reduced to observation of $\boldsymbol{h}_{\text{in}}$.

The magnitude of $\boldsymbol{h}$ and the relationship between $\boldsymbol{h}$ and $\hat{\boldsymbol{b}}$ are invariant from one reference frame to another. Hence, from corresponding quantities in the body-reference frame, the magnitude $\|\boldsymbol{h}_{\text{in}}\|$ and the component of $\boldsymbol{h}_{\text{in}}$ along $\hat{\boldsymbol{b}}_{\text{in}}$ are known, which leaves only one unknown component of $\boldsymbol{h}_{\text{in}}$. Because external torques are assumed to be negligible, $\boldsymbol{h}_{\text{in}}$ remains fixed in inertial coordinates. If $\hat{\boldsymbol{b}}_{\text{in}}$ moves between measurements, then the projection of $\boldsymbol{h}_{\text{in}}$ onto the span of two measurements may be calculated from the component along each measurement. This situation is shown in Fig. 3. The component of $\boldsymbol{h}_{\text{in}}$ orthogonal to the plane spanned by $\hat{\boldsymbol{b}}_{\text{in}}(t_1)$ and $\hat{\boldsymbol{b}}_{\text{in}}(t_2)$ may be calculated from knowledge of $\|\boldsymbol{h}_{\text{in}}\| = \|\boldsymbol{h}_{\text{sc}}\|$, to within a sign uncertainty. Any $\hat{\boldsymbol{b}}_{\text{in}}$ at a third time that moves out of the plane resolves the sign uncertainty.

The key point here is that movement of $\hat{\boldsymbol{b}}_{\text{in}}$ in inertial space is crucial to observation of $\boldsymbol{x} = [\boldsymbol{h}_{\text{in}}^T, \alpha_1, \alpha_2, \theta]^T$. Of course, very small movements of $\hat{\boldsymbol{b}}_{\text{in}}$ result in weak state observability, whereas larger transits approaching 90 deg strengthen the observation.

Because of a short flight duration, the SIERRA subpayloads do not enjoy large excursions of $\hat{\boldsymbol{b}}_{\text{in}}$. The total change in the magnetic field direction over 700 s of data capture is less than 14 deg. Weak observability in this case demands accuracy in the a priori momentum estimate, $\hat{\boldsymbol{h}}_{\text{in}(0)}$. (The circumflex here denotes an estimate, not a unit vector as for $\hat{\boldsymbol{b}}_{\text{sc}}$.) Errors in the magnitude of $\hat{\boldsymbol{h}}_{\text{in}(0)}$ and in its component along $\hat{\boldsymbol{b}}_{\text{in}}$ are readily corrected by magnetometer measurements, whereas errors orthogonal to the plane spanned by $\{\hat{\text{h}}_{\text{in}(0)}, \hat{\boldsymbol{b}}_{\text{in}}\}$ are not immediately visible because they constitute rotation of $\hat{\boldsymbol{h}}_{\text{in}(0)}$ about $\hat{\boldsymbol{b}}_{\text{in}}$. They can be corrected only through movement of $\hat{\boldsymbol{b}}_{\text{in}}$.

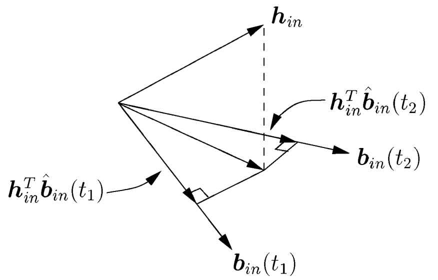

Fig. 3 Relationship between $\boldsymbol{h}_{\text{in}}$ and the magnetic field vector at times t_1 and t_2.

Dynamics and Kinematics Models

In the case of the SIERRA subpayloads, no control torques or significant environmental forces act on the spacecraft, so angular momentum is nearly conserved from one time step to the next. This fact, coupled with inclusion of $\boldsymbol{h}_{\text{in}}$ directly in the estimator state vector, leads to a very simple spacecraft dynamics model:

$$\boldsymbol{h}_{\text{in}(k+1)} = \boldsymbol{h}_{\text{in}(k)} + \boldsymbol{w}_k \tag{13}$$

The impulse $\boldsymbol{w}_k$ is a process noise term that accounts for disturbance torques. For the kinematics model, implicit trapezoidal integration is used to equate the angular rate with the eigenvector of rotation $\boldsymbol{e}$ and the average angular rate over the interval (t_k, t_{k+1}),

$$\frac{\boldsymbol{\omega}_{k+1}\left(\boldsymbol{h}_{\text{sc}(k+1)}\right) + \boldsymbol{p}_{k+1} + \boldsymbol{\omega}_k\left(\boldsymbol{h}_{\text{sc}(k)}\right) + \boldsymbol{p}_k}{2} = \left[\frac{\psi(\boldsymbol{s}_{k+1}, \boldsymbol{s}_k)}{t_{k+1} - t_k}\right]\boldsymbol{e}(\boldsymbol{s}_{k+1}, \boldsymbol{s}_k) \tag{14}$$

Here, the attitude portion of the estimator state vector has been abbreviated into the vector $\boldsymbol{s}_k$

$$\boldsymbol{s}_k = [\alpha_{1(k)}, \alpha_{2(k)}, \theta_k]^T$$

The vector $\boldsymbol{e}(\boldsymbol{s}_{k+1}, \boldsymbol{s}_k)$ is the unit vector in the direction of the Euler rotation that takes the system from attitude $\boldsymbol{s}_k$ to attitude $\boldsymbol{s}_{k+1}$, and the angle $\psi(\boldsymbol{s}_{k+1}, \boldsymbol{s}_k)$ is the magnitude of this rotation. In Ref. 9 expressions are given for both of these quantities. Also note that, because $\boldsymbol{h}_{\text{sc}(k)} = A[\boldsymbol{q}(\boldsymbol{s}_k)]\boldsymbol{h}_{\text{in}(k)}$, the angular rate terms $\boldsymbol{\omega}_{k+1}$ and $\boldsymbol{\omega}_k$ on the left-hand side of Eq. (14) are dependent on $\boldsymbol{s}_{k+1}$ and $\boldsymbol{s}_k$.

The vectors $\boldsymbol{p}_{k+1}$ and $\boldsymbol{p}_k$ play a key role in accommodating the errors in the approximate function $\boldsymbol{\omega}(\boldsymbol{h}_{\text{sc}})$ that result from the simplified model of boom motion, where in-plane boom angles are assumed to be zero and out-of-plane boom angles are such that the booms are orthogonal to $\boldsymbol{h}_{\text{sc}}$. To the degree that spacecraft motion departs from uniform nutation, these approximations of boom motion are less valid, introducing more error into the $\boldsymbol{h}_{\text{sc}}$ to $\boldsymbol{\omega}$ conversion. Because $\boldsymbol{\omega}$ is not included as an element of the state, application of the kinematic model in Eq. (14) requires calculation of $\boldsymbol{h}_{\text{sc}} = A[\boldsymbol{q}(\alpha_1, \alpha_2, \theta)]\boldsymbol{h}_{\text{in}}$ and conversion from $\boldsymbol{h}_{\text{sc}}$ to $\boldsymbol{\omega}$ via $\boldsymbol{\omega}(\boldsymbol{h}_{\text{sc}})$. The noise parameters $\boldsymbol{p}_{k+1}$ and $\boldsymbol{p}_k$ account for the errors introduced by this conversion.

Note that, because the noise sequence $\boldsymbol{p}_k$ corresponds to macroscopic motion of the booms, it will be time correlated. The estimator does not model any correlation of the $\boldsymbol{p}_k$ sequence, but its use of both $\boldsymbol{p}_{k+1}$ and $\boldsymbol{p}_k$ on the left-hand side of Eq. (14) constitutes a correlated model of the effect on the kinematics of this error sequence. This is further explained in the subsequent filter development.

Measurement Model

When the spacecraft attitude is parameterized based on the magnetometer measurement $\hat{\boldsymbol{b}}_{\mathrm{sc}}$, as in Ref. 9, an uncomplicated measurement model results:

$$\begin{bmatrix} 0 \\ 0 \end{bmatrix} = \begin{bmatrix} \mathbf{0} & 1 & 0 & 0 \\ \mathbf{0} & 0 & 1 & 0 \end{bmatrix} \begin{bmatrix} \boldsymbol{h}_{\mathrm{in}(k)} \\ \alpha_{1(k)} \\ \alpha_{2(k)} \\ \theta_k \end{bmatrix} + \tilde{\boldsymbol{\nu}}$$

$$= \tilde{C}\boldsymbol{x}_k + \tilde{\boldsymbol{\nu}} \tag{15}$$

The 2×1 vector $\tilde{\boldsymbol{\nu}}$ represents measurement noise. The measurement model implies that, in the absence of noise, the parameters α_1 and α_2 are identically zero and that the true and measured magnetic field vectors in Fig. 2 are exactly aligned. Subsumed into $\tilde{\boldsymbol{\nu}}$ are contributions from several error sources including sensor noise, quantization noise, spacecraft position error, and geomagnetic field model error. The discrete sequence $\tilde{\boldsymbol{\nu}}$ is modeled as zero-mean uncorrelated Gaussian noise with covariance

$$E\left[\tilde{\boldsymbol{\nu}}_k \tilde{\boldsymbol{\nu}}_j^T\right] = \left[\sigma_{\tilde{\nu}}^2 I_{2\times 2}\right]\delta_{k,j} = P_{\tilde{\nu}\tilde{\nu}}\delta_{k,j} \tag{16}$$

Filtering

The discrete-time square-root information filter described here is based on material drawn from Refs. 9 and 12. Departures from the filter presented in Ref. 9 are those required to incorporate the new state vector in which $\boldsymbol{h}_{\mathrm{in}}$ replaces $\boldsymbol{\omega}$ and to incorporate the new model error sequence $\boldsymbol{p}_k$. The results of this paper are not dependent on a square-root implementation of the filter and smoother: an extended Kalman filter implementation would be equally effective. This is because roundoff errors are much less significant than modeling errors in the SIERRA attitude estimation problem.

In the following, the overbar indicates an a priori estimate: an estimate of the state $\boldsymbol{x}_k$ based on measurements up to time t_{k-1}. The circumflex denotes an a posteriori estimate: an estimate of the state $\boldsymbol{x}_k$ based on measurements up to time t_k. The filtering algorithm proceeds as follows:

1) Given an a posteriori state estimate

$$\hat{\boldsymbol{x}}_k = \left[\hat{\boldsymbol{h}}_{\mathrm{in}(k)}^T, \hat{\alpha}_{1(k)}, \hat{\alpha}_{2(k)}, \hat{\theta}_k\right]^T = \left[\hat{\boldsymbol{h}}_{\mathrm{in}(k)}^T, \hat{\boldsymbol{s}}_k^T\right]^T$$

the attitude portion of the state, $\hat{\boldsymbol{s}}_k$, is used to convert $\hat{\boldsymbol{h}}_{\mathrm{in}(k)}$ to spacecraft coordinates: $\hat{\boldsymbol{h}}_{\mathrm{sc}(k)} = A[\boldsymbol{q}(\hat{\boldsymbol{s}}_k)]\hat{\boldsymbol{h}}_{\mathrm{in}(k)}$. The relation $\boldsymbol{\omega}(\boldsymbol{h}_{\mathrm{sc}})$ is then applied to obtain $\hat{\boldsymbol{\omega}}_k$ in spacecraft coordinates. A quaternion of rotation $\boldsymbol{q}_{\mathrm{rot}}(\hat{\boldsymbol{\omega}}_k, \Delta t_k)$ is formed from $\hat{\boldsymbol{\omega}}_k$ and $\Delta t_k = t_{k+1} - t_k$. It describes the rotation during the sampling interval, assuming $\boldsymbol{\omega}$ is constant. This is used to construct the quaternion

$$\boldsymbol{q}(\bar{\boldsymbol{s}}_{k+1}) = \boldsymbol{q}_{\mathrm{rot}}(\hat{\boldsymbol{\omega}}_k, \Delta t_k) \otimes \boldsymbol{q}(\hat{\boldsymbol{s}}_k) \tag{17}$$

from which $\bar{\theta}_{k+1}$ may be extracted assuming a priori values $\bar{\alpha}_{1(k+1)} = \bar{\alpha}_{2(k+1)} = 0$, as described in Eqs. (28–30) of Ref. 9. The a priori angular momentum $\bar{\boldsymbol{h}}_{\mathrm{in}(k+1)}$ is calculated from Eq. (13) assuming $\boldsymbol{w}_k = 0$. The full a priori state estimate is then

$$\bar{\boldsymbol{x}}_{k+1} = \left[\bar{h}_{\mathrm{in}(k+1)}^T, 0, 0, \bar{\theta}_{k+1}\right]^T$$

2) Equations (13) and (14) are each linearized about both $\hat{\boldsymbol{x}}_k$ and $\bar{\boldsymbol{x}}_{k+1}$ to produce the mapping equation

$$\boldsymbol{x}_k = \Phi_k \boldsymbol{x}_{k+1} + \Gamma_k \boldsymbol{w}_k + \Lambda_{k,k}\boldsymbol{p}_k + \Lambda_{k,k+1}\boldsymbol{p}_{k+1} + \xi_k \tag{18}$$

where ξ_k is a known nonhomogeneous term.

3) Information equations are constructed from the measurement model in Eq. (15) and from noise models for $\boldsymbol{w}_k$ and $\boldsymbol{p}_{k+1}$. For convenience in working with the square-root information filter, information equations are square-root normalized such that the noise terms are distributed as $\sim N(0, I)$. For example, Eq. (15) is premultiplied by $R_{\tilde{\nu}\tilde{\nu}}$ where $(R_{\tilde{\nu}\tilde{\nu}}^T R_{\tilde{\nu}\tilde{\nu}})^{-1} = P_{\tilde{\nu}\tilde{\nu}}$, yielding

$$0 = C\boldsymbol{x}_k + \boldsymbol{\nu}_k \tag{19}$$

with $\boldsymbol{\nu}_k \sim N(0, I)$. Similarly, the information equations for $\boldsymbol{p}_{k+1}$ and $\boldsymbol{w}_k$ are

$$0 = \bar{R}_{pp(k+1)}\boldsymbol{p}_{k+1} + \boldsymbol{\nu}_{p(k+1)} \tag{20}$$

$$0 = \bar{R}_{ww}\boldsymbol{w}_k + \boldsymbol{\nu}_{w(k)} \tag{21}$$

with $\boldsymbol{\nu}_{(.)} \sim N(0, I)$.

4) The state $\boldsymbol{x}_k$ and noise term $\boldsymbol{p}_k$ are combined into an augmented state. The a posteriori information equation for this augmented state from the preceding iteration is

$$\begin{bmatrix} z_{p(k)} \\ z_{x(k)} \end{bmatrix} = \begin{bmatrix} R_{pp(k)} & R_{px(k)} \\ 0 & R_{xx(k)} \end{bmatrix} \begin{bmatrix} \boldsymbol{p}_k \\ \boldsymbol{x}_k \end{bmatrix} + \begin{bmatrix} \boldsymbol{\nu}_{p(k)} \\ \boldsymbol{\nu}_{x(k)} \end{bmatrix} \tag{22}$$

again with $\boldsymbol{\nu}_{(.)} \sim N(0, I)$. The a posteriori state estimate $\hat{\boldsymbol{x}}_k$ and error covariance $P_{xx(k)}$ are related to this information equation by

$$\hat{\boldsymbol{x}}_k = R_{xx(k)}^{-1} z_{x(k)}, \qquad P_{xx(k)} = \left(R_{xx(k)}^T R_{xx(k)}\right)^{-1}$$

To perform time and measurement updates from time t_k to t_{k+1}, the square-root information filter minimizes the following least-squares cost function subject to the linearized dynamics mapping equation (18):

$$\boldsymbol{J} = \left\| \begin{bmatrix} z_{p(k)} \\ z_{x(k)} \end{bmatrix} - \begin{bmatrix} R_{pp(k)} & R_{px(k)} \\ 0 & R_{xx(k)} \end{bmatrix} \begin{bmatrix} \boldsymbol{p}_k \\ \boldsymbol{x}_k \end{bmatrix} \right\|^2 + \left\| \bar{R}_{pp(k+1)}\boldsymbol{p}_{k+1} \right\|^2$$

$$+ \|\bar{R}_{ww}\boldsymbol{w}_k\|^2 + \|C\boldsymbol{x}_{k+1}\|^2 \tag{23}$$

Minimization of J is equivalent to maximization of the state vector's a posteriori conditional probability density function, making the current least-squares formulation a maximum a posteriori estimator. Combining the cost functional terms and eliminating $\boldsymbol{x}_k$ via Eq. (18) leads to

$$\boldsymbol{J} = \left\| \begin{bmatrix} R_{pp(k)} + R_{px(k)}\Lambda_{k,k} & R_{px(k)}\Gamma_k & R_{px(k)}\Lambda_{k,k+1} & R_{px(k)}\Phi_k \\ 0 & \bar{R}_{ww} & 0 & 0 \\ 0 & 0 & \bar{R}_{pp(k+1)} & 0 \\ R_{xx(k)}\Lambda_{k,k} & R_{xx(k)}\Gamma_k & R_{xx(k)}\Lambda_{k,k+1} & R_{xx(k)}\Phi_k \\ 0 & 0 & 0 & C \end{bmatrix} \right.$$

$$\left. \times \begin{bmatrix} \boldsymbol{p}_k \\ \boldsymbol{w}_k \\ \boldsymbol{p}_{k+1} \\ \boldsymbol{x}_{k+1} \end{bmatrix} - \begin{bmatrix} z_{p(k)} - R_{px(k)}\xi_k \\ 0 \\ 0 \\ z_{x(k)} - R_{xx(k)}\xi_k \\ 0 \end{bmatrix} \right\|^2 \tag{24}$$

5) An orthogonal transformation found by QR factorizing the large block matrix in Eq. (24) is applied to both terms within the vector norm, triangularizing the block matrix without affecting the magnitude of the overall vector norm,

$$\boldsymbol{J} = \left\| \begin{bmatrix} R_{pp(k)}^* & R_{pw(k)}^* & R_{p(k)p(k+1)}^* & R_{p(k)x(k+1)}^* \\ 0 & R_{ww(k)}^* & R_{w(k)p(k+1)}^* & R_{w(k)x(k+1)}^* \\ 0 & 0 & R_{pp(k+1)} & R_{px(k+1)} \\ 0 & 0 & 0 & R_{xx(k+1)} \\ 0 & 0 & 0 & 0 \end{bmatrix} \begin{bmatrix} \boldsymbol{p}_k \\ \boldsymbol{w}_k \\ \boldsymbol{p}_{k+1} \\ \boldsymbol{x}_{k+1} \end{bmatrix} \right.$$

$$\left. - \begin{bmatrix} z_{p(k)}^* \\ z_{w(k)}^* \\ z_{p(k+1)} \\ z_{x(k+1)} \\ \epsilon_{k+1} \end{bmatrix} \right\|^2 \tag{25}$$

The matrices on the diagonal of the large block matrix in Eq. (25) are all square, nonsingular, and upper-triangular. The asterisk refers to quantities that will be used to do smoothing.

6) The a posteriori state estimate $\hat{\boldsymbol{x}}_{k+1}$ is solved for using $\hat{x}_{k+1} = R_{xx(k+1)}^{-1} z_{x(k+1)}$. The quantity $\|\boldsymbol{\epsilon}_{k+1}\|^2$ represents the sum of the squared errors in the least-squares fit. The third and fourth lines of Eq. (25), which are like Eq. (22), are extracted for use in the next filter iteration, with k replaced by $k+1$.

An important feature of the filtering algorithm is the evolution of the noise vector $\boldsymbol{p}_k$. At time step k, information equation (20) effectively resets $\boldsymbol{p}_{k+1}$, modeling it as being uncorrelated with earlier values of $\boldsymbol{p}_k$. However, as can be seen in the structure of Eqs. (22) and (25), an a posteriori estimate of $\boldsymbol{p}_{k+1}$ forms part of the augmented state in the information equation for the next iteration. Note that an extended Kalman filter formulation of the filtering algorithm must likewise include the three elements of $\boldsymbol{p}_k$ in an augmented state vector. This one-step-memory process implements a time correlation model of the error in Eq. (14).

Fixed Interval Smoothing

The smoother problem formulation and solution algorithm use the same discrete-time square-root information structure as the filtering problem. The smoother performs a backwards pass on the data, taking as initial estimates the terminal estimates $\hat{\boldsymbol{x}}_N$ and $\hat{\boldsymbol{p}}_N$ provided by the filter. Equation (18), inverted to express $\boldsymbol{x}_{k+1}$ in terms of $\boldsymbol{x}_k$, is used as the mapping equation for the backward pass. At each time step, information equations for smoothed estimates $\hat{\boldsymbol{x}}_{k+1|0:N}$ and $\hat{\boldsymbol{p}}_{k+1|0:N}$ are available in the form of Eq. (22) from the preceding iteration. (The subscript notation employed here refers to the smoothed estimate at $k+1 \in [0, N]$ based on all data from 0 to N.) These are combined with a posteriori data from iteration $k+1$ of the filtering pass by replacing the third and fourth lines of Eq. (25) with the R matrices and z vectors that are associated with $\hat{\boldsymbol{x}}_{k+1|0:N}$ and $\hat{\boldsymbol{p}}_{k+1|0:N}$. The quantity $\boldsymbol{x}_{k+1}$ is eliminated from the resulting cost by using Eq. (18) to solve for $\boldsymbol{x}_k$ in terms of $\boldsymbol{x}_{k+1}$, $\boldsymbol{w}_k, \boldsymbol{p}_k$, and $\boldsymbol{p}_{k+1}$. Finally, an appropriate orthogonal transformation is applied as in step 5 of the filter to yield smoothed information equations for $\hat{\boldsymbol{x}}_{k|0:N}$ and $\hat{\boldsymbol{p}}_{k|0:N}$ that are independent of $\boldsymbol{w}_k$ and $\boldsymbol{p}_{k+1}$. The process is then repeated.

Filter Tuning

The process of filter tuning consists in choosing values for the a priori statistical models represented by matrices $R_{\tilde{\nu}\tilde{\nu}}$, $\bar{R}_{pp(k)}$, $\bar{R}_{ww}$, $R_{pp(0)}$, $R_{px(0)}$, and $R_{xx(0)}$, along with an initial state estimate $\hat{\boldsymbol{x}}_0$. (Because the smoother relies on a posteriori filter statistics, no additional smoother-specific tuning is required.) The tuning process typically proceeds by first relating parameter values to physical phenomena and then adjusting these values to achieve satisfactory filter performance as measured by truth-model simulation and innovations analysis.

The matrix $R_{\tilde{\nu}\tilde{\nu}}$, used to develop Eq. (19), is the square root of the inverse covariance of the zero-mean measurement noise $\tilde{\boldsymbol{\nu}}_k$. The statistics of $\tilde{\boldsymbol{\nu}}_k$ must account for geomagnetic field model errors as well as sensor and quantization noise. Model errors may be approximated by comparing a 7th-order, 1995 geomagnetic model against a 10th-order, year 2000 model. Sensor and quantization noise are modeled for the SIERRA subpayload magnetometers as a random measurement error with a standard deviation of 0.4 deg in each of the two axes orthogonal to the measured magnetic field. These are combined with the field model errors for a standard deviation of $\sigma_{\tilde{\nu}} = 0.0077$ rad. Recall by Eq. (11) that the parameters α_1 and α_2 correspond to one-half of the total rotation about $\hat{\boldsymbol{v}}_1$ and $\hat{\boldsymbol{v}}_2$, respectively. The matrix $R_{\tilde{\nu}\tilde{\nu}}$ is formed as

$$R_{\tilde{\nu}\tilde{\nu}} = \sigma_{\tilde{\nu}}^{-1} I_{2\times 2}$$

For simplicity, the time correlation in the slowly varying geomagnetic field model error is not included in the filter, but it is included in the truth model that has been used to test the filter.

The process noise $\boldsymbol{w}_k$ represents a torque impulse impingent on the spacecraft over the sample period. It is related to physical phenomena. Solar radiation pressure, gravity-gradient torques, and atmospheric drag torques are the primary disturbance factors over the altitude range of the SIERRA subpayloads. The square-root information matrix $\bar{R}_{ww}$ is related to $\boldsymbol{w}_k$ by

$$E[\boldsymbol{w}_j \boldsymbol{w}_k] = \left(\bar{R}_{ww}^T \bar{R}_{ww}\right)^{-1} \delta_{j,k}$$

The matrix $\bar{R}_{ww}$ is assumed diagonal with identical elements, that is,

$$\bar{R}_{ww} = \sigma_w^{-1} I_{3\times 3}$$

The tuned value of σ_w is 10^{-4} N · m · s. This value has been selected based on the expected levels of the disturbance sources listed earlier.

The vector $\boldsymbol{p}_k$ models the error in the conversion from $\boldsymbol{h}_{\mathrm{sc}}$ to $\boldsymbol{\omega}$ through the function $\boldsymbol{\omega}(\boldsymbol{h}_{\mathrm{sc}})$. The statistics of the sequence $\boldsymbol{p}_k$ depend on the richness of the spacecraft's modal excitation. The approximations in $\boldsymbol{\omega}(\boldsymbol{h}_{\mathrm{sc}})$ are more exact as the spacecraft motion more closely approximates pure nutation. For example, multimodal excitation in a typical test case led to sinusoidal $\boldsymbol{\omega}(\boldsymbol{h}_{\mathrm{sc}})$ errors with an amplitude of 0.1 rad/s, or 1% of the nominal 10-rad/s spin rate, whereas errors when the nutational mode acted alone were about 10 times smaller. A good model for the $\boldsymbol{p}_k$ sequence must take into account both the decay in nonnutational spacecraft modes (and the consequent decrease in the error $\boldsymbol{p}_k$) and the nominal intensity of $\boldsymbol{p}_k$ when in pure nutation. The equation governing the time dependence of $\bar{R}_{pp(k)}$ has been formulated as

$$\bar{R}_{pp(k)} = \sigma_{p(k)}^{-1} I_{3\times 3}, \qquad \sigma_{p(k)} = \sigma_f + (\sigma_0 - \sigma_f)\exp(-t_k/\tau) \quad (26)$$

The parameter σ_0 reflects the magnitude of errors in $\boldsymbol{\omega}(\boldsymbol{h}_{\mathrm{sc}})$ immediately following boom deployment, whereas σ_f represents errors after the stable-boom articulation modes have decayed to zero. Selection of values for these parameters is guided by a comparison of truth-model data for $\boldsymbol{\omega}_k$ against the approximation $\boldsymbol{\omega}(\boldsymbol{h}_{\mathrm{sc}(k)})$ under the type of postdeployment multimodal excitation that might be expected. The time constant τ is chosen close to the decay time constants of significant nonnutational modes. The selected parameter values for the SIERRA subpayloads are

$$\sigma_0 = 0.4 \text{ rad/s}, \qquad \sigma_f = 0.03 \text{ rad/s}, \qquad \tau = 100 \text{ s}$$

The time correlation in the error in Eq. (14) is modeled by using the one-step memory process whereby $\boldsymbol{p}_k$ and $\boldsymbol{p}_{k+1}$ both appear in the equation. A more exotic exponentially correlated process has also been tested, with unremarkable improvement. The one-step memory process was selected because it requires a minimal number of tuning parameters while capturing the bulk of the time correlation. The square-root information matrix $\bar{R}_{pp(k)}$ is related to $\boldsymbol{p}_k$ by

$$E\left[\boldsymbol{p}_k \boldsymbol{p}_k^T\right] = \left(\bar{R}_{pp(k)}^T \bar{R}_{pp(k)}\right)^{-1}$$

The diagonal elements of $R_{xx(0)}$ are chosen to be commensurate with expected errors in the initial state estimate $\hat{\boldsymbol{x}}_0$, and the off-diagonal elements are set to 0. The matrix $R_{pp(0)}$ is set equal to $\bar{R}_{pp(0)}$, whereas $R_{px(0)}$ is set to 0, reflecting the assumption that $\boldsymbol{p}_0$ and the errors in $\hat{\boldsymbol{x}}_0$ are uncorrelated.

Adjustments to the tuning values have been made to match the modeled covariances with filter performance. The sequence of residuals $\boldsymbol{\epsilon}_k$ in Eq. (25) is used as the performance metric in this process. In the absence of modeling errors, the sequence $\boldsymbol{\epsilon}_k$ is distributed as

$$E[\boldsymbol{\epsilon}_k] = 0, \qquad E\left[\boldsymbol{\epsilon}_k \boldsymbol{\epsilon}_j^T\right] = I_{2\times 2}\delta_{k,j} \quad (27)$$

An average of $\|\boldsymbol{\epsilon}_k\|^2$ over K time steps may be written

$$\bar{\epsilon}_K = \frac{1}{K}\sum_{i=1}^{K} \|\boldsymbol{\epsilon}_i\|^2 \quad (28)$$

From this it may be noted that $K\bar{\epsilon}_K \sim \chi^2_{(2K)}$. The matrices $R_{xx(0)}$, $\bar{R}_{pp(k)}$, and $\bar{R}_{ww}$ have been tuned so that the weighted average $K\bar{\epsilon}_K$ is near the 95% confidence bounds of the $\chi^2_{(2K)}$ distribution. This process worked well when using simulated data but was less effective with empirical data where high-frequency errors in the measurement were insignificant compared with the slowly varying magnetic field model errors. This resulted in smaller innovations than expected because the filter was able to fit the low-frequency noise better than the high-frequency noise model predicted. The final strategy adopted was to tune the filter by using simulated data and then to vary only $R_{xx(0)}$ when tuning the filter to empirical data, choosing the $R_{xx(0)}$ that gave a good overall fit to the measurements while maintaining $\bar{\boldsymbol{h}}_{\text{in}}$ fairly constant. The tuned values of $\bar{R}_{pp(k)}$ and $\bar{R}_{ww}$ are as noted earlier and the tuned value of $R^{-1}_{xx(0)} = \text{diag}([1, 1, 1, 0.01, 0.01, 0.01])$. The magnitude of the angular momentum vector for each subpayload is more than 20 $\text{N} \cdot \text{m} \cdot \text{s}$. The three 1 values for the initial angular momentum component error standard deviations are less than 5% of this magnitude.

IV. Results When the Filter and Smoother Operate on Simulated Data

Truth-Model Simulation

The truth-model simulator employs the dynamics model of Ref. 2, which governs the time evolution of the 23-element state vector $\boldsymbol{x}$ presented in Sec. II. It models the spacecraft attitude and rate and the relative boom positions and rates. Runge–Kutta integration is used to solve for $\boldsymbol{x}(t_k)$. To validate the simulator output, the total system angular momentum was reconstructed for the zero-torque case. This was shown to be constant over 700 s of simulated data.

A realistic simulation of the sensor noise is important to truth-model testing of an estimation algorithm. Errors in magnetometer measurements are of two categories: sensor errors and magnetic field model errors. Sensor errors relating to nonorthogonality, scale factor errors, and biases are not included in the simulator output. It is assumed that these errors are removed by calibration during the data preparation process. It is further assumed that magnetometer mounting misalignment is calibrated before launch. The remaining sensor errors are nondeterministic thermal noise and quantization noise. These can be lumped together and modeled as a discrete-time zero-mean white Gaussian process. It is important to consider the sampling interval when selecting the value of the process variance because more closely spaced samples are less likely to be uncorrelated. This effect can be modeled loosely by increasing the variance of the uncorrelated noise added to simulate the measurement. The sampling rate of the magnetometer measurements produced by the simulator was set at 120 Hz to match the sampling rate of the SIERRA magnetometers. The magnetometer sampling rate must be at least twice the angular frequency of the rotating spacecraft to avoid aliasing. Higher sampling rates generally improve the performance of the estimator as long as the increased correlation in the noise from one measurement to the next is accounted for in the measurement model.

For the current simulator, a zero-mean uncorrelated error angle with a standard deviation of 0.57 deg is added to each magnetometer measurement to simulate thermal and quantization noise within the magnetometer. Comparison with SIERRA flight data has shown this to be a pessimistic estimate of high-frequency noise, but it has been adopted so that the simulation cases will be demanding. Time-tagging errors in the magnetometer measurements for the SIERRA subpayloads were not modeled because these are a negligible fraction of the sampling interval.

To simulate magnetic field model errors, which include errors in spacecraft position knowledge within the geomagnetic field, a 10th-order, year 2000 International Geomagnetic Reference Field (IGRF) is used as the truth model, whereas a 7th-order 1995 IGRF model is used in the filter/smoother. This strategy captures the time correlation inherent in the magnetic field model errors. The field is calculated at the Earth-relative positions of the SIERRA flight trajectory. Hence, the simulated magnetic field movement reflects the actual 13.6-deg rotation of the true magnetic field during the data collection period of the SIERRA mission.

Representative Results

A 700-s data segment was created using the SIERRA simulator under the following conditions:

1) The initial spacecraft angular rate $\omega_0 = 10.14$ rad/s.

2) The initial nutation angle $= 1.8$ deg, and the final nutation angle $= 10.4$ deg.

3) The initial angle between $\boldsymbol{h}_{\text{in}}$ and $\boldsymbol{b}_{\text{in}} = 34$ deg. This angle is related to the sensitivity of the attitude estimate to errors in the estimate of $\boldsymbol{h}_{\text{in}}$. Maximal (minimal) sensitivity occurs for $\boldsymbol{h}_{\text{in}}$ and $\boldsymbol{b}_{\text{in}}$ aligned (orthogonal). Although the actual SIERRA subpayloads enjoy a robust 87- and 97-deg separation, a narrower angle was chosen in simulation to represent a less ideal situation.

4) The total angular rotation of $\boldsymbol{b}_{\text{in}} = 13.6$ deg.

5) The error in the initial estimate of attitude parameter $\theta = 5.7$ deg.

6) The error in the initial $\boldsymbol{h}_{\text{in}}$ estimate consists of three equal components: one in the $\{\boldsymbol{h}_{\text{in}}, \boldsymbol{b}_{\text{in}}\}$ plane and perpendicular to $\boldsymbol{h}_{\text{in}}$, one orthogonal to the plane, and one along $\boldsymbol{h}_{\text{in}}$. The magnitude of each error component is 5% of the magnitude of $\boldsymbol{h}_{\text{in}(0)}$. These lead to an initial $\boldsymbol{h}_{\text{in}(0)}$ estimate 4 deg from the true angular momentum.

Estimation results for the filter and smoother using simulated data are presented in Figs. 4–6. Figure 4 shows the total error angle in the attitude estimates produced by the filter and the smoother over a 700-s run. The effect of the nonnutational modes is evident in the first 300 s in which the attitude estimation errors undergo larger excursions than during the remaining 400 s. The smoothed total attitude error angle remains below 4 deg throughout the run. It drops below 2 deg as multimodal motion gives way to pure nutation, causing approximations within the estimator to become more accurate.

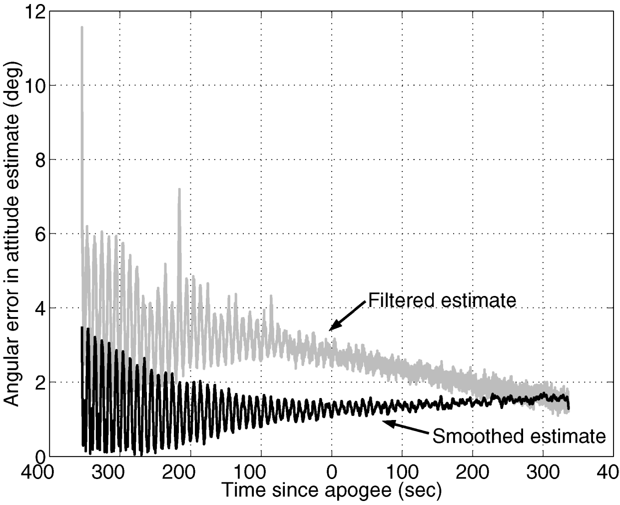

Fig. 4 Filtered and smoothed total attitude error angle for a 700-s run with simulated data.

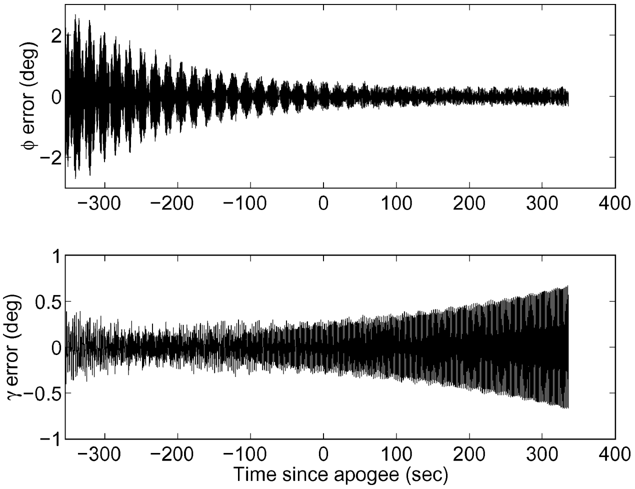

Fig. 5 Errors in the smoothed estimates of the angles ϕ_1 and γ_1 for a 700-s run with simulated data (representative of errors in all four booms).

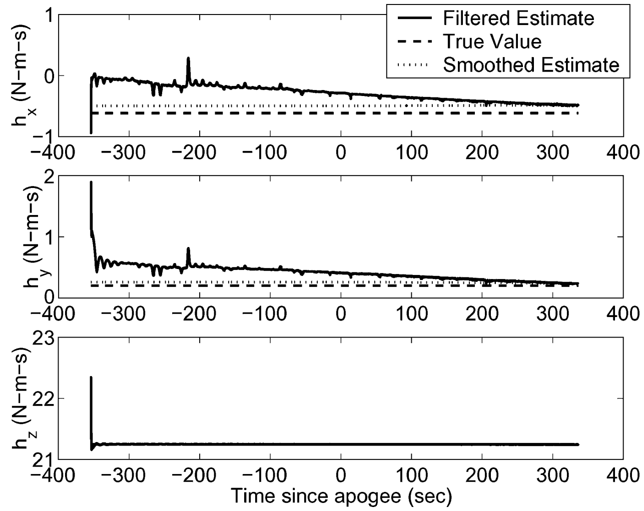

Fig. 6 Filtered and smoothed estimates of $\boldsymbol{h}_{\rm in}$ components compared with values from the truth-model simulation for a 700-s run by using simulated data.

Figure 5 presents the errors in the smoothed estimates of the boom articulation angles ϕ_1 and γ_1. These are representative of the errors in all four booms. Errors in the out-of-plane angle ϕ_1 fall below 0.5 deg after nonnutational modes die out, validating the assumption that the booms lie approximately perpendicular to the angular momentum vector during pure nutation. Errors in the in-plane boom angle γ_1 reflect the deviation from the assumed value of zero. These errors increase as the spacecraft nutation angle grows. Analysis shows that this instability of the in-plane boom angles is due to the boom attachment points being slightly displaced along the z direction from the system center of mass. As the spacecraft nutates, the in-plane motion of the booms' base attachment points produces a periodic in-plane forcing, which acts to increase the in-plane boom articulation angles γ_i. For nutation angles below 15 deg, the in-plane boom deflection remains below 1 deg.

The filtered and smoothed estimates of the inertial angular momentum components are compared with the true component values in Fig. 6. The z component of $\hat{\boldsymbol{h}}_{\rm in}$ contains less error than the x and y components. This is because $\boldsymbol{h}_{\rm in}$ is nearly aligned along the reference z axis, so that corrections to the magnitude of $\hat{\boldsymbol{h}}_{\rm in}$ are reflected in the z component of $\hat{\boldsymbol{h}}_{\rm in}$. As has been mentioned, the magnitude of $\boldsymbol{h}_{\rm in}$ is a strongly observable quantity, which is why the filter is able to correct the z component of $\hat{\boldsymbol{h}}_{\rm in}$ almost immediately. The large initial x- and y-component corrections in Fig. 6 are along the other most observable direction, which is in the $\{\boldsymbol{h}_{\rm in}, \boldsymbol{b}_{\rm in}\}$ plane. The key to the remaining gradual improvement in the filtered angular momentum estimate is the movement of $\boldsymbol{b}_{\rm in}$ in inertial space. Additional information about $\boldsymbol{h}_{\rm in}$ is revealed as $\boldsymbol{b}_{\rm in}$ changes its direction. Because knowledge of $\boldsymbol{h}_{\rm in}$ is linked to attitude knowledge, the attitude estimate is also refined.

Herein lies the significance of including $\boldsymbol{h}_{\rm in}$ directly as an element of the state. Under the conditions of weak observability brought on by using only a magnetometer and by the small 13.6-deg rotation of $\boldsymbol{b}_{\rm in}$, incremental information gathered about $\boldsymbol{h}_{\rm in}$ must be closely guarded. It was found that a more traditional estimator state, where $\boldsymbol{\omega}$ describes rate, allows errors in the $\boldsymbol{\omega}(\boldsymbol{h}_{\rm sc})$ conversion to creep into the angular momentum, making a reconstruction of $\boldsymbol{h}_{\rm in}$ wander in inertial space, contrary to conservation of angular momentum. This drives the spacecraft attitude estimate into divergence.

One may easily contrast a filter dynamics model based on a state vector that includes $\boldsymbol{\omega}$ and one based on a state vector that instead includes $\boldsymbol{h}_{\rm in}$ for the SIERRA estimation problem. One way to do this is to provide each dynamics model with an error-free initial state and propagate this state forward without measurement updates. These open-loop estimates are then compared to the output of the SIERRA truth-model simulator primed with the same initial state.

The significant deficiencies in both the $\boldsymbol{\omega}$- and $\boldsymbol{h}_{\rm in}$-based dynamics models are due to errors in the relation $\boldsymbol{\omega}(\boldsymbol{h}_{\rm sc})$. These errors arise because the underpinning assumptions of Eqs. (2) and (3) are inexact, especially for subpayload motion that includes modes other than pure nutation. A comparison of the propagation accuracy of these two models has been carried out with the initial conditions described at the beginning of this subsection. These initial conditions lead to subpayload motion that is not purely nutational. It was found that the open-loop state estimate produced by the $\boldsymbol{\omega}$-based model diverged within 10 s. In contrast, the $\boldsymbol{h}_{\rm in}$-based model produced open-loop attitude estimates that strayed only 16 deg from the truth-model attitude after 100 s of propagation. Thus, the use of the inertial angular momentum components as states of the SIERRA filter improves the filter's accuracy by decreasing its dynamics propagation errors.

In any Euler-based estimation scheme, there will exist small errors in the relationship between $\boldsymbol{\omega}$ and $\boldsymbol{h}_{\rm sc}$ owing to factors such as uncertainty in the inertia matrix or in the motion of flexible appendages. Under conditions of strong attitude observability, these errors are corrected soon after they arise, which means that an unforced $\boldsymbol{h}_{\rm in}$ remains fixed in inertial space. In these cases, a traditional state vector employing $\boldsymbol{\omega}$ is adequate. Under weak observability, however, use of $\boldsymbol{h}_{\rm in}$ is preferred. The trivial propagation of Eq. (13) isolates the estimate of $\boldsymbol{h}_{\rm in}$ from errors in $\boldsymbol{\omega}(\boldsymbol{h}_{\rm sc})$.

V. Filter and Smoother Results for SIERRA Flight Data

Data Preparation

Several data preprocessing tasks were carried out before applying the new estimation algorithm to the SIERRA flight data. The raw 1-kHz magnetometer measurements from the TAMs onboard the SIERRA subpayloads were interpolated and undersampled at 120 Hz. The data were further processed to remove the effects of magnetometer nonorthogonality, scale factor errors, and biases. Obvious measurement outliers were also removed. Biases in the inertial sensors onboard the primary SIERRA payload were calibrated postlaunch by using magnetic field data. Rate measurements from these inertial sensors were used to calculate an initial estimate of $\boldsymbol{h}_{\rm in}$ for each subpayload at separation. This estimate is denoted by $\hat{\boldsymbol{h}}_{\rm in(0)}$.

The remaining estimator state elements, $\alpha_{1,2}$ and θ, were initialized as follows: Elements $\alpha_{1,2}$ assumed their a priori value of 0. Rotation θ was chosen such that initial transients in the estimate of $\boldsymbol{h}_{\rm in}$ were as smooth as possible. This is equivalent to the hypothesis testing approach used in Ref. 9, where selection of the initial θ is driven by the size of the resulting innovations process.

The size of the error in $\hat{\boldsymbol{h}}_{\rm in(0)}$ may be inferred from the corrections applied to $\hat{\boldsymbol{h}}_{\rm in(0)}$ by the filter and the smoother. For the fore subpayload, the direction of the smoothed estimate of $\boldsymbol{h}_{\rm in}$ differs from that of the initial estimate by 3.35 deg. The discrepancy for the aft subpayload is more severe: 10.5 deg. This implies that aft results may be less accurate.

Results

Filter and smoother results using telemetered data from the fore subpayload are presented in Figs. 7–9. Figure 7 shows that the angular momentum estimate remains relatively constant over the data capture interval. Thus, the initial angular momentum estimate agrees well with the 700 s of magnetometer data. In Fig. 8, the root-sum-square sequence of the half-angles α_1 and α_2 is plotted for the smoother. These are similar to filter innovations, giving a measure of how well the smoother fits the magnetometer data. Their small size, corresponding to a root-sum-square magnetometer error angle less than 1.2 deg, indicates a close fit to the data. Closer inspection reveals strong time correlation among the innovations. This correlation is probably an artifact of the time-correlated errors in the spacecraft dynamics model and in the magnetic field model errors. Further error modeling might reduce correlation in the innovations sequence, but this was not considered necessary given the satisfactory estimator performance.

In Fig. 9, the smoothed estimate of the out-of-plane boom angle ϕ_1 is presented as representative of estimates for all four booms. Its profile shows the effect of the increasing nutation angle on out-of-plane boom displacement.

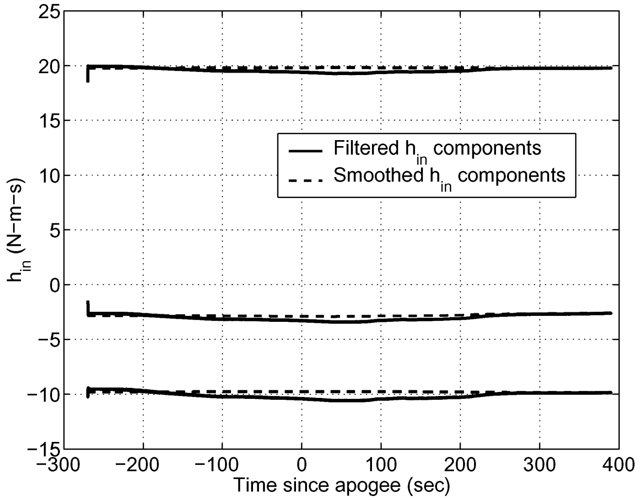

Fig. 7 Components of the filtered and smoothed estimates of h_{in} with data from SIERRA fore subpayload.

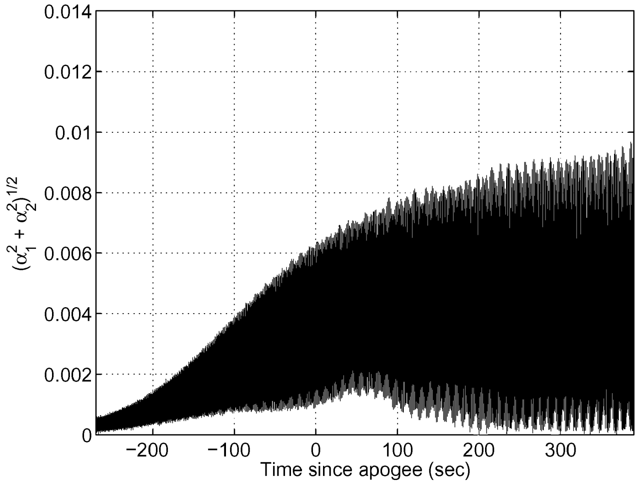

Fig. 8 Root-sum-square of the residual measurement error sequence for smoother applied to flight data.

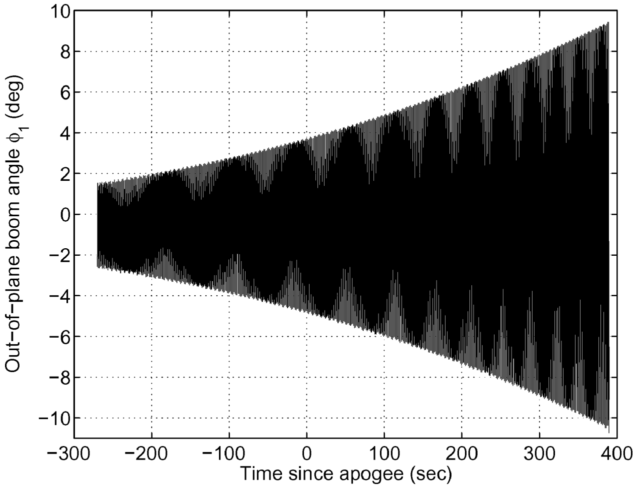

Fig. 9 Smoothed estimate of the out-of-plane boom angle ϕ_1 for SIERRA fore subpayload (representative of all ϕ_i).

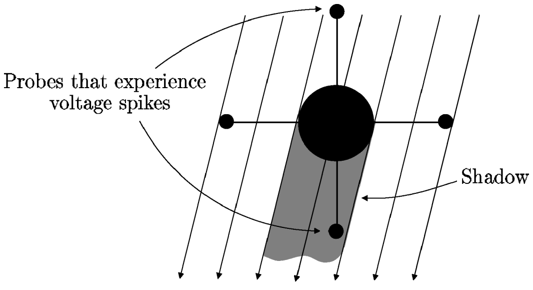

Fig. 10 Plasma shadowing effect.

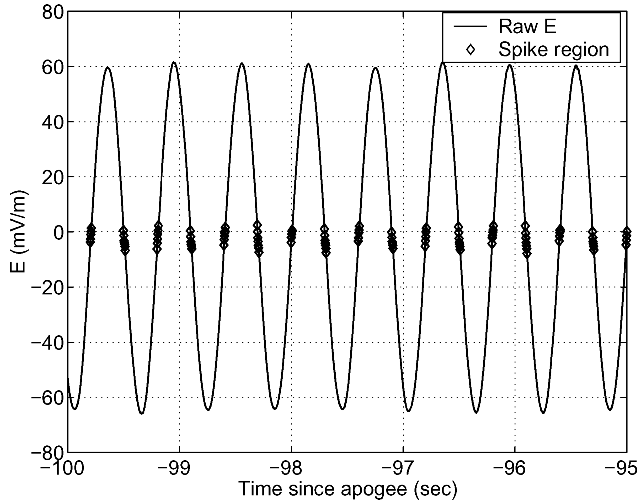

Fig. 11 Electric field measurements between opposite probes of aft SIERRA subpayload.

Independent Check

An independent measure of estimator performance may be formulated from natural ionospheric phenomena. The booms of the SIERRA subpayloads were set up to make electric field measurements between opposite probes. The electric field sensed by the wire probes is the sum of two components. One is an induced electric field $\boldsymbol{E}_{v\times b}=\boldsymbol{v}\times\boldsymbol{b}$ generated by the spacecraft moving in the magnetic field. The other is the ambient electric field present in the ionosphere. For both sources, the electric field is null in the direction of the magnetic field. This is evident for the first source from the cross product operation. For the ambient field, it is a consequence of the high plasma conductivity along magnetic field lines. In practice, however, when opposite booms are aligned along the magnetic field, the body of the spacecraft blocks plasma movement from the region of one probe to the other. This gives rise to a difference in plasma population, and, hence, a voltage potential, between the probes. This plasma shadowing effect manifests itself in voltage spikes in the electric potential measurements. The situation is illustrated in Fig. 10.

If performing properly, the present estimator should be able to predict boom alignments with the magnetic field and, thereby, predict the occurrence of the voltage spikes. This test was carried out, and the estimator was able to predict the voltage spikes accurately. Results for the aft payload are presented in Fig. 11. The marked regions of Fig. 11 are those where predictions of boom and magnetic field alignment to within 5 deg coincide with the small voltage spikes resulting from the plasma shadowing effect. This coincidence provides an independent verification of the boom angle estimates.

Note that the voltage spikes can also be predicted, though less successfully, with only magnetometer data while assuming boom angles $\phi_i=\gamma_i=0$. The added predictive accuracy of the estimator suggests that estimates of boom angles are fairly accurate.

VI. Broadened Scope of Application of the Estimation Algorithms

Modeling errors, time varying and otherwise, are common to the general problem of Euler-based spacecraft attitude estimation. When they are significant, errors can quickly accumulate to the point of destabilizing an estimator that has weak state observability. The present estimator is designed to accommodate time-varying model uncertainty and weak state observability. It does this by directly including $\boldsymbol{h}_{\text{in}}$ in the estimator state and by allowing random error in the relationship between $\boldsymbol{\omega}$ and $\boldsymbol{h}_{\text{sc}}$. This technique is useful for spacecraft with modest attitude knowledge requirements where flexible appendages, uncertain inertia parameters, or both, could foul a traditional Euler-based Kalman filter. It is also useful as a backup estimator should sensors (for example, gyros) fail, and Euler-based estimation becomes a last resort.

VII. Conclusions

A magnetometer-based attitude estimation filter and smoother have been developed for a spinning spacecraft with wire booms. The new estimator overcomes two principal challenges: significant time-varying modeling errors and weak state observability. This is done by including the inertially referenced angular momentum vector directly as a state element and by expressly accounting for modeling errors within the spacecraft kinematics. These random modeling errors enter the algebraic relationship whereby the spacecraft-referenced angular velocity is determined as a function of the spacecraft-referenced angular momentum. An additional feature of the estimator is that an approximation has been used for this relationship, one that is useful when the spacecraft is undergoing its principal mode of motion, an unstable flexible-body nutation.

The estimator is initialized with an estimate of the system angular momentum and thereafter uses magnetic field measurements to estimate accurately the spacecraft attitude, the angular momentum, and the relative positions of the wire booms. Testing has been carried out by using a full-order nonlinear truth model. Under realistic error and noise conditions, the estimator converged to within 2 deg of the true spacecraft attitude. Relative boom orientation estimates remained within 1 deg of the true orientations.

The estimator has also been tested using flight data telemetered from the subpayloads of a recent sounding rocket mission. In this case, the estimator for each subpayload is initialized with an angular momentum estimate based on measurements from inertial sensors onboard the primary payload taken immediately before the deployment of each subpayload. Measurement residuals from the estimator indicate that it is able to fit the subpayloads' magnetometer measurements to within 1.2 deg. An independent test of the estimator performance using electric field measurements has demonstrated the estimator's ability to accurately predict the relative boom positions. The estimator is recommended for use on spacecraft whose Euler dynamics models contain significant uncertainties due to parameter errors or due to the approximate treatment of flexible-body dynamics effects.

Acknowledgments

This work was supported in part by NASA Grants NAG5-5233, Sounding of the Ion Energization Region: Resolving Ambiguities, and NAG5-12894, Validation of a New Electric Field Instrument, both from the Office of Space Sciences. It was also supported by Grant NAG5-11919, Euler Dynamics-Based Estimation Algorithms for Spacecraft Attitude and Rate Determination, from the NASA Goddard Space Flight Center. Richard Harman was Monitor for the latter grant.

References

[1] Powell, S. P., Klatt, E. M., and Kintner, P. M., "Plasma Wave Interferometry Using GPS Positioning and Timing on a Formation of Three-Sub-Orbital Payloads," *Proceedings of the Institute of Navigation Global Positioning System Conference*, Inst. of Navigation, Washington, DC, 2002, pp. 145–154.

[2] Psiaki, M. L., Kintner, P. M., Jr., and Powell, S. P., "Rapid Energy Dissipation in a Yo–Yo-Type Wire Boom Deployment System," *Journal of Guidance, Control, and Dynamics*, Vol. 23, No. 3, 2000, pp. 483–490.

[3] Psiaki, M. L., Powell, S. P., Klatt, E. M., and Kintner, P. M., Jr., "Practical Design and Flight Test of a Yo–Yo Wire Boom Deployment System," *Proceedings of the AIAA Guidance, Navigation, and Control Conference*, AIAA, Reston, VA, 2003.

[4] Longman, R. W., and Fedor, J. V., "Dynamics and Flexible Spinning Satellites with Radial Wire Antennas," *Acta Astronautica*, Vol. 3, Nos. 1–2, 1976, pp. 17–37.

[5] Psiaki, M. L., Klatt, E. M., Kintner, P. M., Jr., and Powell, S. P., "Attitude Estimation for a Flexible Spacecraft in an Unstable Spin," *Journal of Guidance, Control, and Dynamics*, Vol. 25, No. 1, 2002, pp. 88–95.

[6] Humphreys, T. E., "Attitude Determination for Small Satellites with Modest Pointing Constraints," M.S. Thesis, Dept. of Electrical and Computer Engineering, Utah State Univ., Logan, UT, May 2003.

[7] Psiaki, M. L., Martel, F., and Pal, P. K., "Three-Axis Attitude Determination via Kalman Filtering of Magnetometer Data," *Journal of Guidance, Control, and Dynamics*, Vol. 13, No. 3, 1990, pp. 506–514.

[8] Challa, M., Natanson, G., and Ottenstein, N., "Magnetometer-Only Attitude and Rates for Spinning Spacecraft," *Proceedings of the AIAA/AAS Astrodynamics Specialists Conference*, AIAA, Reston, VA, 2000, pp. 311–321.

[9] Psiaki, M. L., "Global Magnetometer-Based Spacecraft Attitude and Rate Estimation," *Journal of Guidance, Control, and Dynamics*, Vol. 27, No. 2, 2004, pp. 240–250.

[10] Psiaki, M. L., and Oshman, Y., "Spacecraft Attitude Rate Estimation from Geomagnetic Field Measurement," *Journal of Guidance, Control, and Dynamics*, Vol. 26, No. 2, 2003, pp. 244–252.

[11] Lerner, G. M., "Three-Axis Attitude Determination," *Spacecraft Attitude Determination and Control*, edited by J. R. Wertz, D. Reidel, Boston, 1978, pp. 424–426.

[12] Bierman, G. J., *Factorization Methods for Discrete Sequential Estimation*, Academic Press, New York, 1977, pp. 69–76, 115–122, 214–217.